THE JOURNAL OF PHYSICAL CHEMISTRY C

Article

Cite This: J. Phys. Chem. C 2018, 122, 194−206

pubs.acs.org/JPCC

Physical Interpretations of Nyquist Plots for EDLC Electrodes and Devices

Bing-Ang Mei,[†] Obaidallah Munteshari,[†] Jonathan Lau,[‡] Bruce Dunn,[‡] and Laurent Pilon*,[†]

[†]Henry Samueli School of Engineering and Applied Science, Mechanical and Aerospace Engineering Department, University of California at Los Angeles, 420 Westwood Plaza, Los Angeles, California 90095, United States

[‡]Henry Samueli School of Engineering and Applied Science, Materials Science and Engineering Department, University of California at Los Angeles, 410 Westwood Plaza, Los Angeles, California 90095, United States

Supporting Information

ABSTRACT: Electrochemical impedance spectroscopy (EIS) consists of plotting so-called Nyquist plots representing negative of the imaginary versus the real parts of the complex impedance of individual electrodes or electrochemical cells. To date, interpretations of Nyquist plots have been based on physical intuition and/or on the use of equivalent RC circuits. However, the resulting interpretations are not unique and have often been inconsistent in the literature. This study aims to provide unequivocal physical interpretations of electrochemical impedance spectroscopy (EIS) results for electric double layer capacitor (EDLC) electrodes and devices. To do so, a physicochemical transport model was used for numerically reproducing Nyquist plots accounting for (i) electric double layer (EDL) formation at the electrode/electrolyte interface, (ii) charge transport in the electrode, and (iii) ion electrodiffusion in binary and symmetric electrolytes. Typical Nyquist plots of EDLC electrodes were reproduced numerically for different electrode conductivity and thickness, electrolyte domain thickness, as well as ion diameter, diffusion coefficient, and concentrations. The electrode resistance, electrolyte resistance, and the equilibrium differential capacitance were identified from Nyquist plots without relying on equivalent RC circuits. The internal resistance retrieved from the numerically generated Nyquist plots was comparable to that retrieved from the "IR drop" in numerically simulated galvanostatic cycling. Furthermore, EIS simulations were performed for EDLC devices, and similar interpretations of Nyquist plots were obtained. Finally, these results and interpretations were confirmed experimentally using EDLC devices consisting of two identical activated-carbon electrodes in both aqueous and nonaqueous electrolytes.

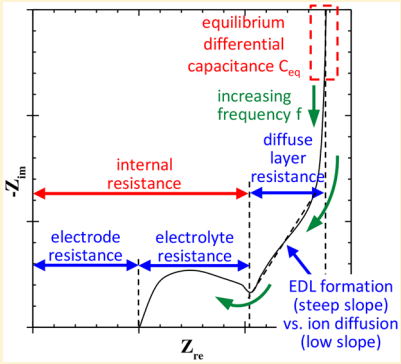

INTRODUCTION

Electrochemical impedance spectroscopy (EIS) has been used extensively to characterize the performance of electrical energy storage and conversion devices including electrochemical capacitors,[1−10] batteries,[11−14] and fuel cells.[15,16] It has also been used to characterize individual electrodes used for electrochemical capacitors,[17−19] corrosion tests,[20,21] and capacitive deionization.[22,23] It consists of imposing a time harmonic oscillating electric potential $\psi_s(t)$ of small oscillation amplitude (e.g., less than 10 mV) around a time-independent "DC potential" at the electrode surfaces and measuring the resulting harmonic current density $j_s(t)$.[7,8,16] Using complex notations, the imposed electric potential $\psi_s(t)$ and the resulting current density $j_s(t)$ can be expressed as[16,24−26]

$$\psi_s(t) = \psi_{dc} + \psi_0 e^{i2\pi ft} \quad \text{and} \quad j_s(t) = j_{dc} + j_0 e^{i[2\pi ft - \phi(f)]} \tag{1}$$

where ψ_{dc} is the time-independent DC potential, ψ_0 is the amplitude of the oscillating potential at frequency f, j_{dc} is the time-independent DC current density, j_0 is the amplitude of the oscillating current density, and $\phi(f)$ is the frequency-dependent phase angle between the imposed potential $\psi_s(t)$ and the measured current density $j_s(t)$. Then, the electrochemical impedance Z can be defined as[16,24−26]

$$Z = \frac{\psi_s(t) - \psi_{dc}}{j_s(t) - j_{dc}} = \frac{\psi_0}{j_0} e^{i\phi} = Z_{re} + iZ_{im} \tag{2}$$

where Z_{re} and Z_{im} (expressed in $\Omega\ m^2$) are the real and imaginary parts of the complex impedance, respectively.

Electric double layer capacitors (EDLC) consist of two porous carbon electrodes separated by liquid electrolyte consisting of a salt dissolved in an aqueous or organic solvent. The electrodes typically consist of activated carbon particles with inner pores less than 2 nm in diameter. Figure 1 shows the schematic of a typical Nyquist plot presenting the imaginary part, $-Z_{im}$, as a function of the real part, Z_{re}, of the complex impedance of an electric double layer capacitor (EDLC). It consists of a semicircle at high frequencies between points A and B, a nonvertical line at intermediate frequencies between points B and C, and a nearly vertical line at low frequencies beyond point C.

Received: October 26, 2017
Revised: December 5, 2017
Published: December 5, 2017

ACS Publications © 2017 American Chemical Society

DOI: 10.1021/acs.jpcc.7b10582
J. Phys. Chem. C 2018, 122, 194−206

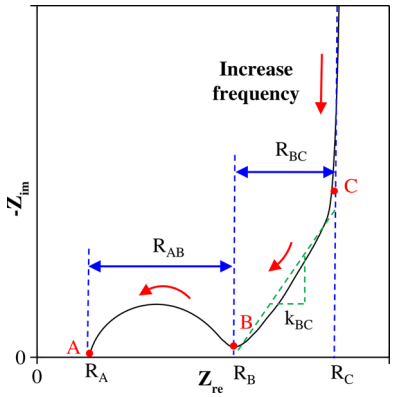

Figure 1. Schematic of typical Nyquist plots for EDLC electrodes or devices.

Multiple and often contradictory physical interpretations of experimental Nyquist plots of EDLCs have been proposed in the literature.[2,27−40] For example, the resistance R_A at point A (Figure 1) has been attributed to (i) the bulk electrolyte resistance[27−33] or (ii) the equivalent series resistance (ESR) also known as the internal resistance defined as the sum of the resistances of the bulk electrolyte, the electrode, and the contact resistance between the electrode and the current collector.[2,34−37] The diameter of the semicircle $R_{AB} = R_B - R_A$ (Figure 1) has been assigned to (i) the electrolyte resistance in the pores of the electrodes,[31,34,35] (ii) the contact resistance between electrode and current collector,[38] (iii) the sum of the electrode resistance and contact resistance between the electrode and the current collector,[32] or (iv) the so-called charge transfer resistance.[27,30] For EDLC devices, the charge transfer resistance corresponds to the sum of the electrolyte resistance in the porous structure of the electrode, the electrode resistance, and the contact resistance between the electrode and the current collector.[30] Based on this interpretation along with the previous interpretation of R_A as the bulk electrolyte resistance,[27−33] the resistance R_B (Figure 1), i.e., $R_B = R_A + R_{AB}$, can be interpreted as the internal resistance, i.e., the sum of bulk electrolyte resistance and the so-called charge transfer resistance.[27,30,32] Furthermore, the existence of the nonvertical line BC (Figure 1) at intermediate frequencies has been assigned to (i) ion transport limitation in the electrolyte in porous electrode structures,[27−29,32,34,37] (ii) ion transport limitation in the bulk electrolyte,[33] or (iii) nonuniform pathway for ion transport from the bulk electrolyte to the porous electrode surface caused by nonuniform electrode pore size and electrode roughness.[2,36,38] Based on the latter interpretation, the resistance R_{BC} (Figure 1) was called the "equivalent distribution resistance".[2] Finally, the vertical line at low frequencies beyond point C (Figure 1) was attributed to the dominant capacitive behavior of the electric double layer formed at the electrode/electrolyte interface.[31,32,34,35,38] The intersection between the vertical line and the Z_{re} axis, corresponding to R_C (Figure 1) has been termed (i) the internal resistance,[30] (ii) the equivalent series resistance (ESR),[33] or (iii) the overall resistance[34] of the electrode or the device. The multiple and contradictory interpretations of the Nyquist plots listed above for R_A, R_B, R_C, R_{AB}, and R_{BC} are confusing and need clarification.

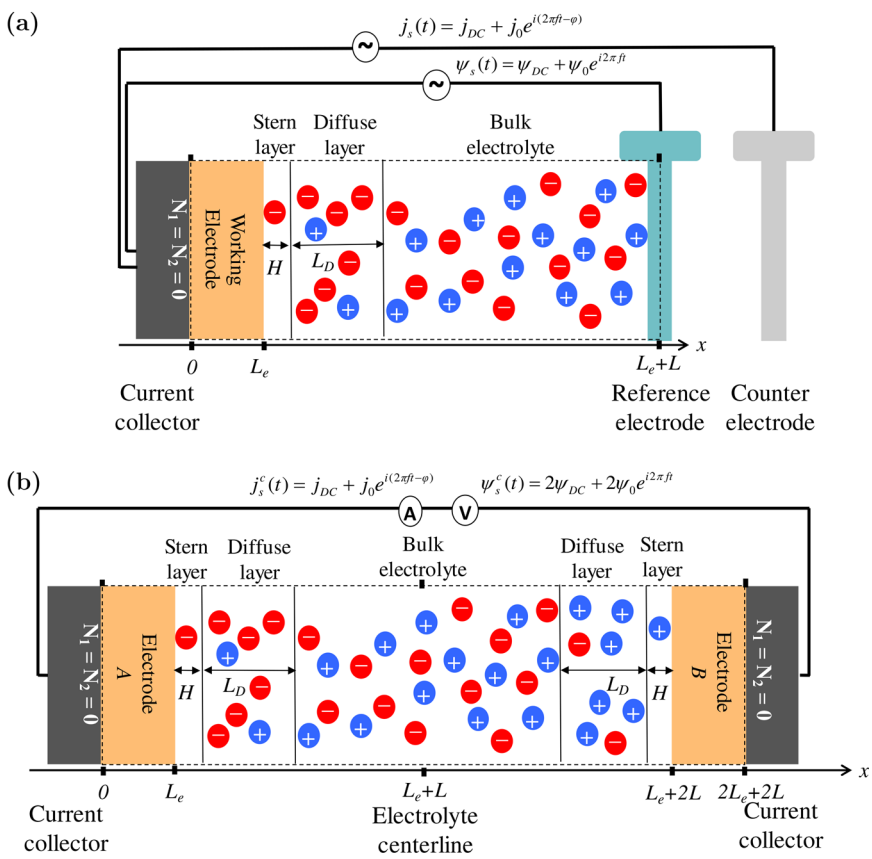

Figure 2. Schematics of (a) the simulated one-dimensional EDLC electrode in a three-electrode setup and (b) EDLC devices consisting of two identical electrodes. The dashed line encloses the computational domain simulated.

DOI: 10.1021/acs.jpcc.7b10582
J. Phys. Chem. C 2018, 122, 194−206

Moreover, equivalent RC circuit models have been commonly used to fit and/or interpret Nyquist plots. They consist of representing EDLC devices or electrodes by an equivalent electric circuit consisting of an arbitrary number of ideal capacitors and resistors.[41−49] Unfortunately, despite their widespread use, equivalent RC circuit models suffer from serious limitations including the facts that (i) they neglect ion diffusion and nonuniform ion concentrations in the electrolyte[47−49] and (ii) two different RC circuit models can produce similarly acceptable impedance response and/or fit experimental data equally well, as demonstrated in the literature.[50,51]

This study aims to provide unequivocal interpretation of Nyquist plots for individual EDLC electrodes and EDLC cells without relying on physical intuition or equivalent RC circuits. To do so, EIS measurements of (i) EDLC electrodes based on three-electrode setup and (ii) two-electrode EDLC cells were numerically reproduced for different electrode conductivity and thickness, different electrolyte domain thickness, as well as for different ion diameter, diffusion coefficient, and concentration in the electrolyte. The study also focuses on retrieving equilibrium differential capacitance and internal resistance from EIS simulations. Finally, the study aims to validate experimentally the physical interpretations of EIS measurements developed numerically using EDLC cells consisting of two identical electrodes made of activated carbon and different aqueous and organic electrolytes.

■ ANALYSIS

Schematic and Assumptions. Figure 2 shows (a) a one-dimensional (1D) simulated domain consisting of a planar current collector supporting a working electrode of thickness L_e and an electrolyte domain of thickness L corresponding to a three-electrode setup and (b) an EDLC device consisting of two identical electrodes of thickness L_e separated by an electrolyte domain of thickness $2L$. The electrolyte near each electrode consisted of a Stern layer of thickness H and a diffuse layer of mobile ions of thickness L_D defined such that $[c_i(x = L_e + H + L_D,t) - c_\infty]/c_\infty \leq 5\%$, where $c_i(x = L_e + H + L_D,t)$ is the local concentration of cations ($i = 1$) or anions ($i = 2$) and c_∞ is the bulk ion concentration. To make the problem mathematically tractable, the following assumptions were made: (1) the electrolyte was binary and symmetric, i.e., it consisted of two ion species of opposite valency $\pm z$ ($z > 0$).[52] The two ion species were further assumed to have identical diameter a and diffusion coefficient D. (2) The Stern layer contained no free charge and its thickness H was approximated as the radius of the ions, so that $H = a/2$, as commonly assumed in continuum simulations of electric double layer.[24,53,54] (3) The transport properties of the electrode and electrolyte were taken as constant. (4) Bulk motion of the electrolyte was negligible. (5) No redox reaction or ion intercalation took place at the surface or within the electrode. (6) Heat generation was ignored and the temperature was uniform and constant in the electrode and electrolyte. (7) Contact resistance between the electrode and the current collector and the electrical resistance of the current collector were negligible. (8) Self-discharge of the electrode or the device was ignored.

Simulations reported in this study were based on the modified Poisson−Nernst−Planck (MPNP) model for binary and symmetric electrolyte for EDLC electrodes or devices. The governing equations, initial and boundary conditions, and method of solution were described in detail in refs 55 and 56 and need not be repeated. The MPNP model governed the spatiotemporal evolution of the potential $\psi(x, t)$ in the electrode and electrolyte as well as the ion concentrations $c_1(x, t)$ of cations and $c_2(x, t)$ of anions in the electrolyte. In addition, the boundary conditions varied depending on whether EIS or galvanostatic cycling were simulated. EIS simulations imposed potential $\psi_s(t)$ at the current collector/electrode interface or across the cell as a harmonic function of time t [eq S.5a]. For galvanostatic cycling, the current density $j_s(t)$ imposed at the current collector/electrode interface or across the cell was a square wave of magnitude j_{GC} with respect to the cycle period [eq S.6]. In single electrode simulations, the potential and the ion concentrations remained as their initial values at the centerline [Figure 2a]. In two-electrode symmetric device simulations, the potential at one current collector/electrode interface was set to zero while the other was at $\psi_s^c(t) = 2\psi_s(t)$ [eq S.5b]. All governing equations along with the initial and boundary conditions, in the 1D coordinate system, shown in Figure 2, were reproduced in the Supporting Information for the sake of completeness.

Constitutive Relationships. In order to solve the coupled transient 1D equations as well as the initial and boundary conditions, a total of 12 parameters were necessary including (i) the electrode electrical conductivity σ_e; (ii) the electrolyte properties ϵ_r, z, a, D, and c_∞; (iii) the dimensions of the simulated electrode and electrolyte domains L_e and L; along with (iv) the operating conditions ψ_{dc}, ψ_0, and f for EIS simulations and ψ_{min}, ψ_{max}, and j_{GC} for galvanostatic cycling, and (v) temperature T (in K). The electrical conductivity σ_e and thickness L_e of the electrode; the electrolyte properties a, D, and c_∞; and the length of the electrolyte domain L were treated as variables to achieve various resistances and capacitances. On the other hand, the temperature was set to room temperature (T = 298 K), and the dielectric constant was taken as that of propylene carbonate, a commonly used organic solvent, i.e., ϵ_r = 64.4.[57] The valency of the ion species was z = 1.[58] Finally, in EIS simulations, the DC potential was set arbitrarily as ψ_{dc} = 0.3 V, the oscillating potential was set as ψ_0 = 5 mV, and the frequency f varied between 0.1 and 5×10^6 Hz. In galvanostatic cycling, the magnitude of imposed current density j_{GC} ranged between 10^{-3} and 1 mA/cm^2 while the potential window was set as ψ_{min} = 0 V and ψ_{max} = 1 V. Table 1 summarizes the values or ranges of these parameters.

Data Processing. *Electrical Resistances.* The electrical resistance R_e (in Ω m^2) per unit surface area of the planar electrode can be expressed as

$$R_e = L_e/\sigma_e \tag{3}$$

To calculate the resistance of the electrolyte, current density due to ion transport in the electrolyte needs to be considered and is given by[1]

$$j(x, t) = zF[N_1(x, t) - N_2(x, t)] \tag{4}$$

where z is the valency, $F = eN_A$ is the Faraday constant, and $N_1(x, t)$ and $N_2(x, t)$ are the mass fluxes of cations and anions in the electrolyte (in mol/m^{2}s) expressed in eq S.3. Note that the local electric field $E(x, t) = -\partial\psi/\partial x$. Thus, the local ionic conductivity $\sigma(x)$ in the electrolyte, defined as $j(x, t) = \sigma(x)E(x, t)$, can be expressed as

$$\sigma(x) = zFD\frac{\partial}{\partial\psi}(c_1 - c_2) + \frac{z^2F^2D(c_1 + c_2)}{R_uT} + \frac{DN_Aa^3(c_1 - c_2)}{1 - N_Aa^3(c_1 + c_2)}\frac{\partial}{\partial\psi}(c_1 + c_2) \tag{5}$$

where D is the diffusion coefficient, $c_1(x, t)$ and $c_2(x, t)$ are the concentrations of cations and anions at location x and time t in

DOI: 10.1021/acs.jpcc.7b10582
J. Phys. Chem. C 2018, 122, 194−206

Table 1. Value or Range of Electrode and Electrolyte Properties and Dimensions Used in the Simulations Reported in This Study

parameter	symbol	value	unit	ref
electrode conductivity	σ_e	5×10^{-8}–5×10^{-5}	S/m	
dielectric constant	ϵ_r	64.4		57
valency	z	1		58
ion diameter	a	0.33–1.32	nm	
diffusion coefficient	D	5×10^{-14}–8×10^{-13}	m^2/s	
bulk ion concentration	c_∞	0.0005–1	mol/L	
electrode thickness	L_e	10–100	nm	
electrolyte thickness	L	40–1600	nm	
DC potential	ψ_{DC}	0.3	V	
amplitude of oscillating potential	ψ_0	5	mV	24–26
frequency	f	0.1–5×10^4	Hz	2,27–40
magnitude of imposed current density	j_{GC}	10^{-3}–0.01	mA/cm^2	
potential window	ψ_{min}	0	V	59
	ψ_{max}	1	V	59
temperature	T	298	K	

Table 2. Simulation Parameters and Corresponding Resistances R_e, R_∞, and R_D and Capacitance $C_{diff,eq}$ [eq 13] and $C_{diff,eq,EIS}$ Values for 25 EIS Simulations for Single Electrodes (Cases 1–24) and an EDLC Cell (Case 25)

case no.	σ_e (S/m)	c_∞ (mol/L)	D (m^2/s)	L (nm)	L_e (nm)	a (nm)	τ_D/τ_{RC}	R_e ($\Omega\ m^2$)	R_∞ ($\Omega\ m^2$)	R_D ($\Omega\ m^2$)	$C_{diff,eq}$ ($\mu F/cm^2$)	$C_{diff,eq,EIS}$ ($\mu F/cm^2$)
2	1×10^{-7}	0.001	2×10^{-13}	160	10	0.66	0.72	0.1	0.105	0.07	94.8	94.8
3	5×10^{-8}	0.001	2×10^{-13}	160	10	0.66	0.68	0.2	0.105	0.07	94.8	95.0
4	5×10^{-5}	0.01	2×10^{-13}	160	10	0.66	7.13	2×10^{-4}	0.0105	0.009	91.5	91.6
5	5×10^{-5}	0.001	2×10^{-13}	160	10	0.66	0.68	2×10^{-4}	0.105	0.07	94.8	94.6
6	5×10^{-5}	0.0005	2×10^{-13}	160	10	0.66	0.37	2×10^{-4}	0.20	0.14	92.7	94.4
7	5×10^{-5}	0.001	2×10^{-13}	80	10	0.66	0.38	2×10^{-4}	0.05	0.04	94.9	92.2
8	1×10^{-7}	0.002	2×10^{-13}	160	10	0.66	1.47	0.1	0.05	0.04	95.5	93.5
9	5×10^{-5}	0.002	5×10^{-14}	80	10	0.66	0.78	2×10^{-4}	0.105	0.09	95.6	93.7
10	5×10^{-5}	0.002	2×10^{-13}	160	10	0.33	0.62	2×10^{-4}	0.05	0.05	206.4	197.1
11	5×10^{-5}	0.0005	8×10^{-13}	320	10	0.66	0.66	2×10^{-4}	0.105	0.10	94.7	93.6
12	5×10^{-5}	0.0005	2×10^{-13}	160	10	1.32	0.91	2×10^{-4}	0.20	0.19	38.1	38.4
13	5×10^{-5}	0.001	2×10^{-13}	80	10	1.32	1.04	2×10^{-4}	0.05	0.04	37.1	36.6
14	5×10^{-5}	0.001	2×10^{-13}	320	10	0.33	0.66	2×10^{-4}	0.20	0.19	194.4	197.4
15	5×10^{-5}	0.001	2×10^{-13}	160	10	1.32	1.84	2×10^{-4}	0.105	0.10	37.1	37.1
16	5×10^{-5}	0.001	2×10^{-13}	160	10	0.33	0.33	2×10^{-4}	0.105	0.10	194.9	197.2
17	5×10^{-5}	0.001	1×10^{-13}	80	10	0.66	0.37	2×10^{-4}	0.105	0.09	94.9	93.0
18	5×10^{-5}	0.0005	1×10^{-13}	160	10	0.66	0.37	2×10^{-4}	0.41	0.40	92.7	88.3
19	5×10^{-5}	0.001	5×10^{-14}	80	10	0.66	0.37	2×10^{-4}	0.20	0.17	94.9	94.9
20	5×10^{-5}	0.001	1×10^{-13}	320	10	0.66	1.39	2×10^{-4}	0.05	0.05	92.7	94.4
21	1×10^{-7}	0.004	2×10^{-13}	160	10	0.66	3.04	0.1	0.03	0.02	95.2	93.4
22	1×10^{-7}	0.006	2×10^{-13}	160	10	0.66	4.34	0.1	0.02	0.02	94.7	93.0
23	5×10^{-5}	0.0075	2×10^{-13}	160	10	0.66	5.50	2×10^{-4}	0.01	0.01	92.3	92.2
24	5×10^{-5}	1	2×10^{-13}	1600	100	0.66	2.09×10^4	2×10^{-3}	1.06×10^{-3}	1.24×10^{-6}	66.5	62.0
25**	5×10^{-5}	1	2×10^{-13}	1600	100	0.66	4.18×10^4	4×10^{-3}	2.12×10^{-3}	2.48×10^{-6}	33.2	31.5

the electrolyte, $\psi(x, t)$ is the potential in the electrolyte, R_u = 8.314 J /mol K is the universal gas constant, a is the effective ion diameter, and N_A is Avogadro's number. Here, the diffuse layer contained mobile ions with nonzero concentration gradients while the ion concentrations in the bulk electrolyte remained constant. Thus, the ionic conductivity $\sigma(x)$ varied with location in the diffuse layer and was a harmonic function of time that could be represented using complex notations. However, it remained constant and real in the bulk electrolyte. The resistance, i.e., the real part of the impedance, of the diffuse layer near one electrode can be expressed as

$$R_D = Re\left[\int_{L_e}^{L_e+L_D} \frac{dx}{\sigma(x)}\right] \tag{6}$$

Note that the local ion concentrations $c_1(x, t)$ and $c_2(x, t)$ in the diffuse layer as well as the diffuse layer thickness L_D were unknown and were determined numerically. Finally, the bulk electrolyte resistance can be expressed as[1]

$$R_\infty = (L - L_D)/\sigma_\infty \quad \text{with} \quad \sigma_\infty = (2z^2F^2Dc_\infty)/(R_uT) \tag{7}$$

where σ_∞ is the electrical conductivity of the bulk electrolyte.

Moreover, for EDLC cells (referred to by superscript "c"), the resistances of the electrodes R_e^c, the diffuse layer R_D^c, and the bulk electrolyte R_∞^c can be expressed as

$$R_e^c = 2R_e \tag{8}$$

DOI: 10.1021/acs.jpcc.7b10582
J. Phys. Chem. C 2018, 122, 194–206

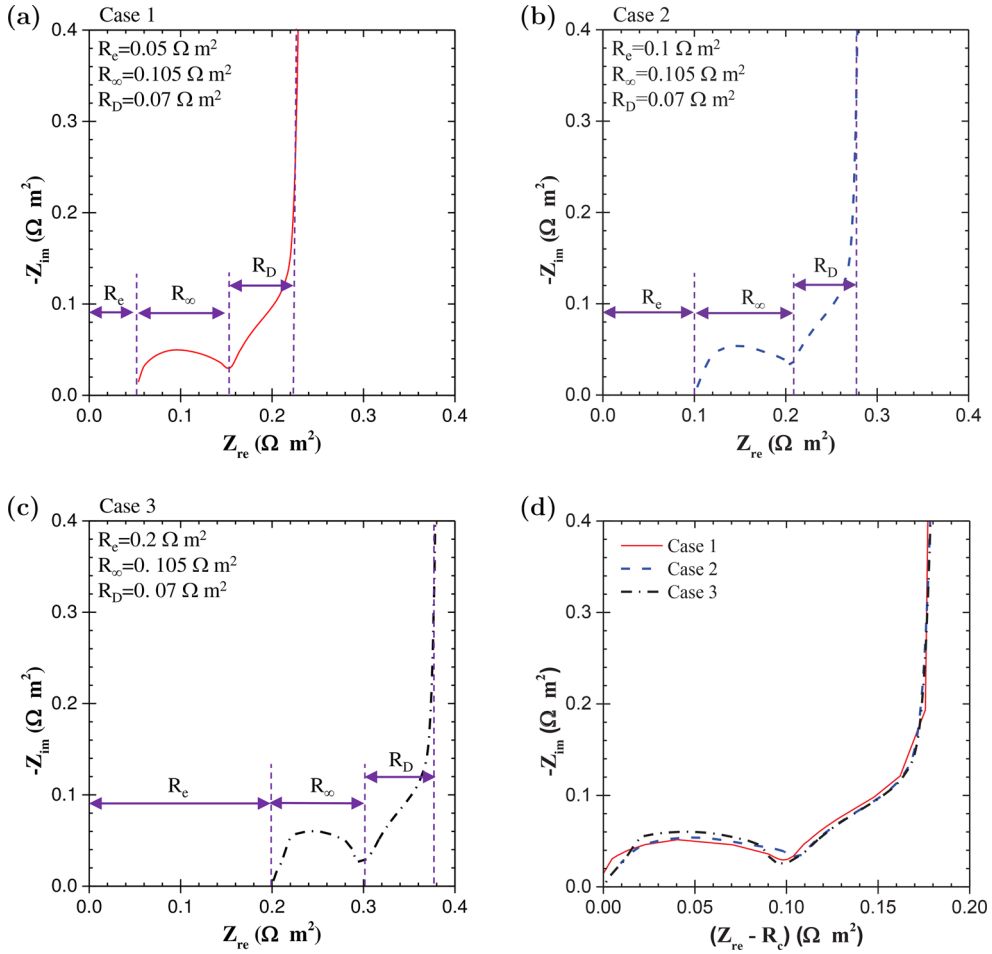

Figure 3. (a−c) Nyquist plots for EDLC electrode for cases 1−3 (Table 2) featuring electrode resistance R_e of (a) 0.05, (b) 0.1, and (c) 0.2 Ω m², as predicted by eq 3. (d) Modified Nyquist plots $-Z_{im}$ versus $Z_{re} - R_e$ for the three cases.

$$R_D^c = Re\left[\int_{L_e}^{L_e+L_D} \frac{dx}{\sigma(x)} + \int_{L_e+2L-L_D}^{L_e+2L} \frac{dx}{\sigma(x)}\right] \tag{9}$$

$$R_\infty^c = 2(L - L_D)/\sigma_\infty \tag{10}$$

Finally, the internal resistance R_{GC} (in Ω m²) retrieved from galvanostatic cycling for both single-electrode and device simulations can be expressed as[60,61]

$$R_{GC}(j_{GC}) = \frac{\Delta\psi}{2j_{GC}} \tag{11}$$

where $\Delta\psi$ is the potential drop observed at the beginning of discharge under constant current density j_{GC}.

Equilibrium Differential Capacitance. The differential capacitance (in μF/cm²) is defined as[1,24,62]

$$C_{diff} = \frac{dq_s}{d\psi_s} \tag{12}$$

where q_s (in C/m²) is the surface charge density. For a given EDLC electrode under equilibrium conditions, it is denoted by $C_{diff,eq}$ and can be expressed as[63,64]

$$\frac{1}{C_{diff,eq}} = \frac{1}{C_{diff,eq}^{St}} + \frac{1}{C_{diff,eq}^{D}} \tag{13}$$

where $C_{diff,eq}^{St}$ and $C_{diff,eq}^{D}$ are the equilibrium differential capacitances of the Stern layer and diffuse layer near the electrode, respectively. They can be expressed as[63,64]

$$C_{diff,eq}^{St} = \frac{\epsilon_0\epsilon_r}{H} \tag{14a}$$

and

$$C_{diff,eq}^{D} = \frac{\frac{\epsilon_0\epsilon_r}{\lambda_D}\sinh\left(\frac{ze\psi_D}{k_BT}\right)}{\left[1 + 2\nu\sinh^2\left(\frac{ze\psi_D}{2k_BT}\right)\right]\sqrt{\frac{2}{\nu}\log\left[1 + 2\nu\sinh^2\left(\frac{ze\psi_D}{2k_BT}\right)\right]}} \tag{14b}$$

where $\lambda_D = [\epsilon_0\epsilon_r k_BT/(2e^2z^2N_Ac_\infty)]^{1/2}$ is the Debye length, e is the elementary charge, and k_B is the Boltzmann constant, respectively. The packing parameter ν is defined as $\nu = 2a^3N_Ac_\infty$. For planar electrode under equilibrium conditions, the electric potential at the Stern/diffuse layer interface, denoted by ψ_D, can be expressed as a function of the potential ψ_s imposed at the electrode/current collector interface according to[65]

$$\frac{\psi_D}{k_BT/ez} = 0.37\left(\frac{\psi_s}{k_BT/ez}\right)^{1.16} \tag{15}$$

DOI: 10.1021/acs.jpcc.7b10582
J. Phys. Chem. C 2018, 122, 194−206

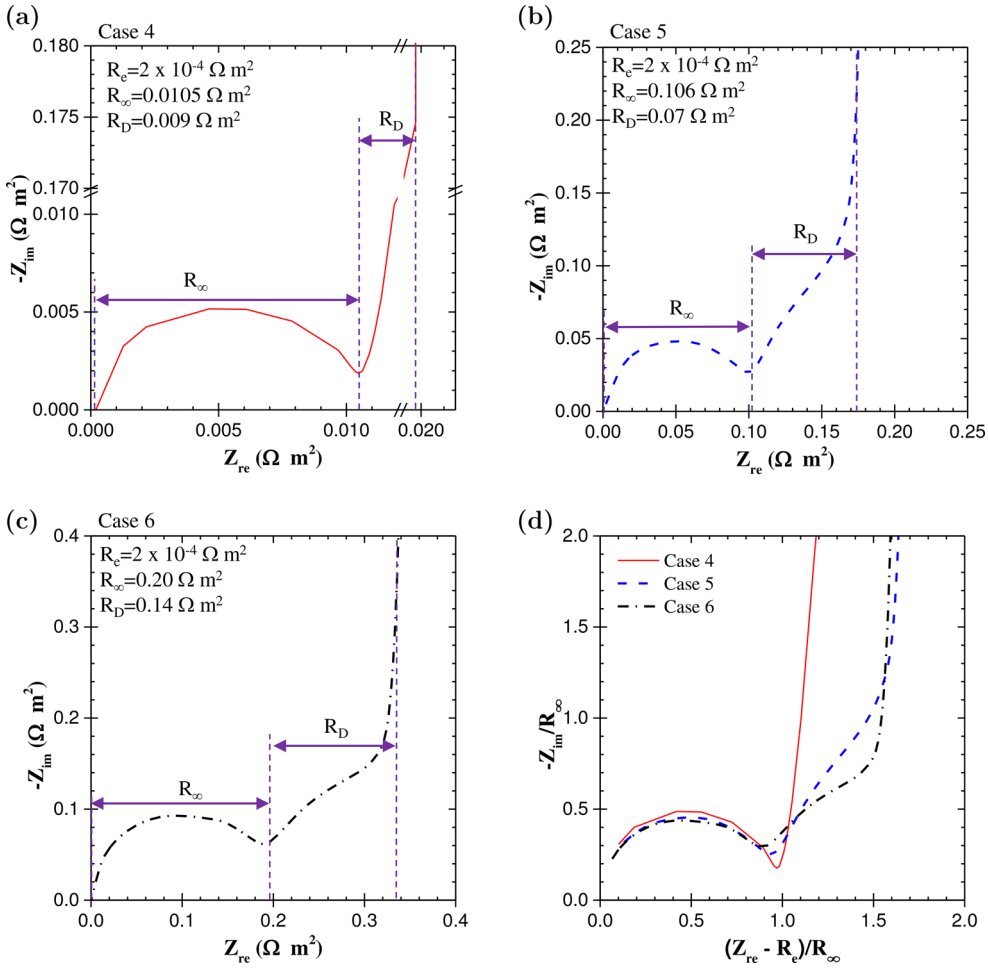

Figure 4. (a−c) Nyquist plots for EDLC electrodes for cases 4−6 (Table 2) featuring bulk electrolyte resistance R_∞ of (a) 0.011, (b) 0.106, and (c) 0.212 Ω m^2, as predicted by eq 7. (d) Dimensionless Nyquist plots $-Z_{im}/R_\infty$ versus $(Z_{re} - R_e)/R_\infty$ for the three cases.

Note that for EIS simulations, ψ_s in eq 15 corresponds to the time-independent potential ψ_{dc}.

Finally, an EDLC cell with two identical electrodes can be treated as two capacitors in series. Thus, the equilibrium capacitance of the EDLC cell can be expressed as $C^c_{diff,eq} = C_{diff,eq}/2$.

RESULTS AND DISCUSSION

Interpretation of the Nyquist Plot for EDLC Electrodes.

Table 2 summarizes the different cases (cases 1−24) considered to assess the effects of electrode and electrolyte resistances and electrode capacitance on the Nyquist plots of a single EDLC electrode.

Electrode Resistance R_e. Figure 3a−c shows the Nyquist plots for EDLC electrodes of cases 1−3 featuring electrode electrical conductivity σ_e of (a) 2×10^{-7}, (b) 1×10^{-7}, and (c) 5×10^{-8} S/m, corresponding to electrode resistance R_e [eq 3] of (a) 0.05, (b) 0.1, and (c) 0.2 Ω m^2, respectively. All other parameters remained the same in these three cases. First, Figure 3a−c resembles remarkably experimental EIS measurements on single EDLC electrodes.[17−19] In addition, they indicate that changing electrode resistance led to a horizontal shift of the Nyquist plot along the Z_{re} axis. Moreover, the high-frequency intersection of the Nyquist plot with the Z_{re} axis (corresponding to R_A in Figure 1) was systematically equal to the electrode resistance R_e predicted by eq 3. Note that the present simulations ignored contact resistance between the electrode and the current collector. However, it can be accounted for as a resistance in series with R_e, and its sole effect on the Nyquist plot would also be to shift the plot along the Z_{re} axis. Note that the so-called "charge-transfer" resistance at the electrode/electrolyte interface associated with redox reactions and sometimes used to interpret EIS measurements for EDLCs[27,30] was absent in our simulations.

Furthermore, Figure 3d shows $-Z_{im}$ as a function of $Z_{re} - R_e$ for the above three cases. It indicates that the Nyquist plots for cases 1−3 nearly collapsed on the same line regardless of changes in electrode conductivity σ_e. In other words, σ_e had no significant effects on the Nyquist plots at low and medium frequencies. In addition, it is interesting to note that the diameter of the semicircle in Figure 3 (corresponding to $R_{AB} = R_B - R_A$ in Figure 1) was equal to the bulk electrolyte resistance R_∞ predicted by eq 7 and equal to 0.105 Ω m^2 in all three cases.

Electrolyte Resistances R_∞ and R_D. To further explore the effect of electrolyte resistances R_∞ and R_D, Figure 4a−c shows the Nyquist plots for EDLC electrodes for cases 4−6 featuring bulk ion concentration c_∞ of (a) 0.01, (b) 0.001, and (c) 0.0005 mol/L, corresponding to bulk electrolyte resistance R_∞ [eq 7] and diffuse layer resistance R_D [eq 6] of (a) 0.01 and 0.009, (b) 0.106 and 0.07, and (c) 0.20 and 0.14 Ω m^2, respectively. All other parameters remained the same in these three cases. Figure 4a−c establishes that the diameter of the semicircle R_{AB} (Figure 1) was equal to the bulk electrolyte resistance R_∞ while the resistance R_{BC} corresponded to the diffuse layer resistance R_D. In fact, the same observations could be retrospectively made in Figure 3.

DOI: 10.1021/acs.jpcc.7b10582
J. Phys. Chem. C 2018, 122, 194−206

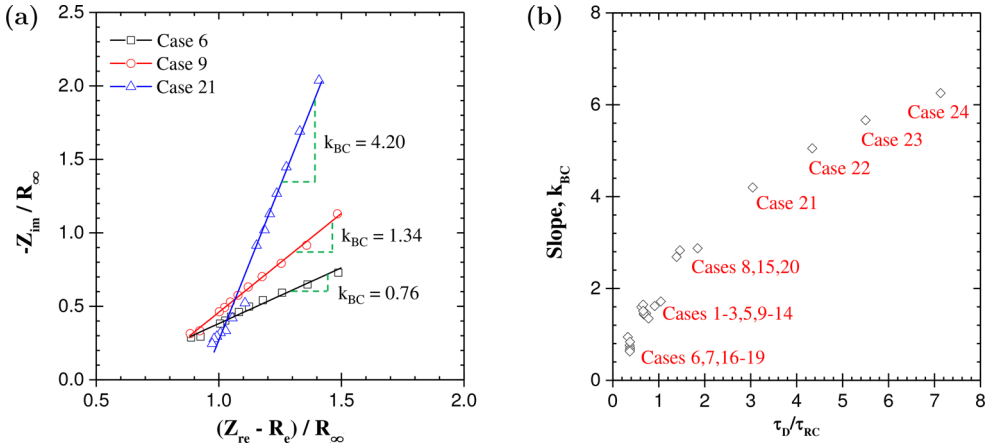

Figure 5. (a) Nonvertical line at intermediate frequencies for cases 6, 9, and 21 (Table 2) for illustration. (b) Slope of the nonvertical line as a function of the time scale ratio τ_D/τ_{RC}.

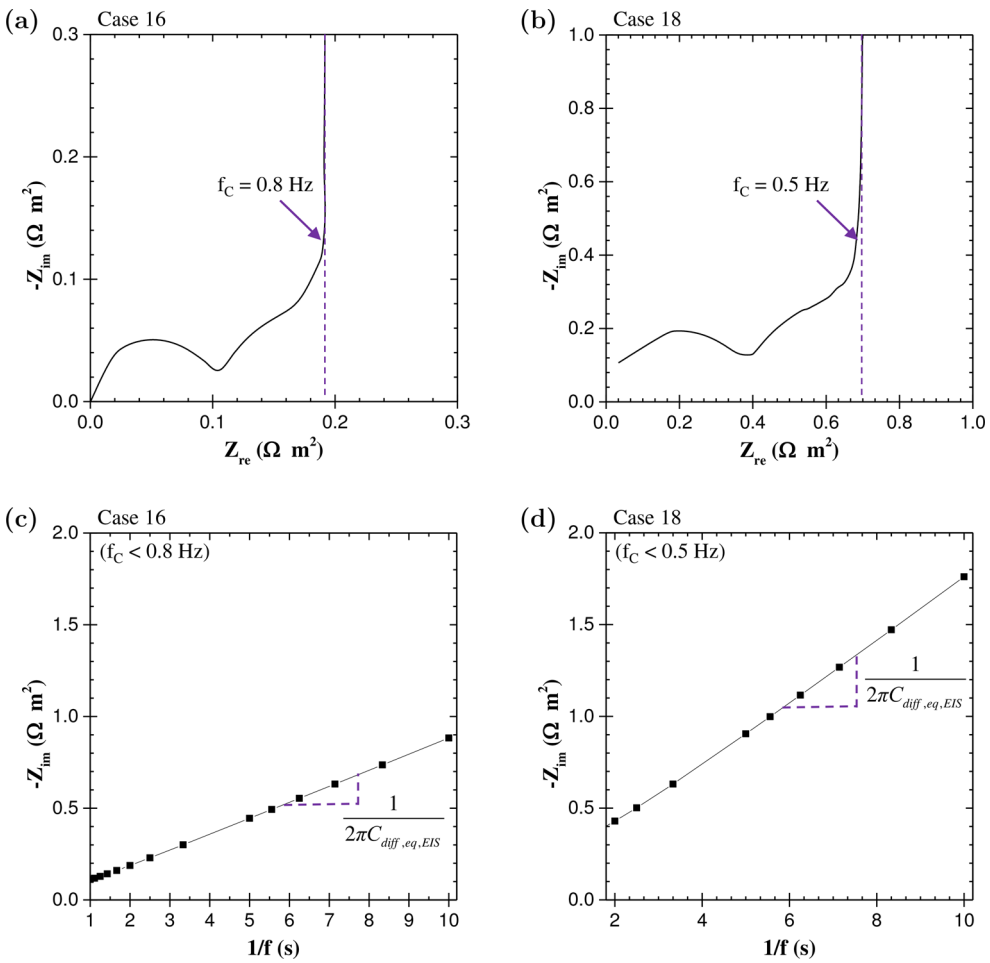

Figure 6. (a and b) Nyquist plots for (a) case 16 and (b) case 18 (Table 2) and (c and d) corresponding imaginary part of the impedance $-Z_{im}$ as a function of $1/f$ for low frequencies. Similar results were obtained for all other cases.

In addition, Figure 4d shows the dimensionless Nyquist plot $-Z_{im}/R_\infty$ versus $(Z_{re} - R_e)/R_\infty$ for the three cases. It indicates that, unlike σ_e, the electrolyte concentration c_∞ had a significant impact on the slope k_{BC} (Figure 1) corresponding to intermediate EIS frequencies.

Moreover, Figure 5a shows the dimensionless Nyquist plot $-Z_{im}/R_\infty$ as a function of $(Z_{re} - R_e)/R_\infty$ for intermediate frequencies ranging between f_C and f_B for cases 6, 9, and 21 in Table 2. The frequency f_B corresponded to the intersection between the semicircle and the nonvertical line (point B in Figure 1) while frequency f_C was such that $f_C \approx f_B/20$ (point C in Figure 1). These three cases were chosen arbitrarily for illustration purposes. The slope k_{BC} was retrieved by least-squares fitting between f_B and f_C for cases 1−23 of Table 2 with coefficient of determination R^2 systematically larger than 0.95. Figure 5b shows the slope k_{BC} as a function of the ratio τ_D/τ_{RC}, for the 23 cases

DOI: 10.1021/acs.jpcc.7b10582
J. Phys. Chem. C 2018, 122, 194−206

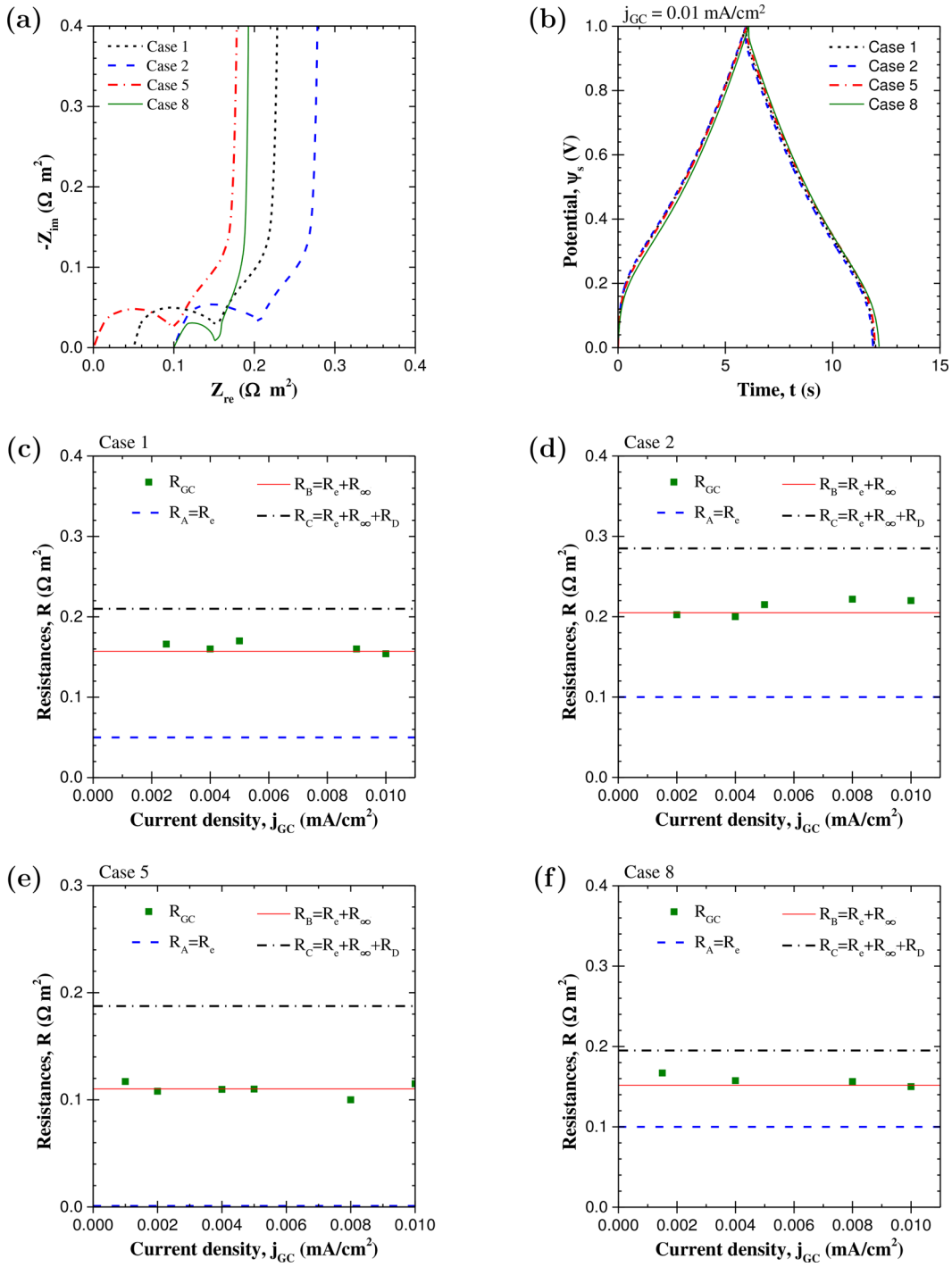

Figure 7. (a) Nyquist plots and (b) potential $\psi_s(t)$ as a function of time under constant current cycling j_{GC} = 0.01 mA/cm^2 for cases 1, 2, 5, and 8 summarized in Table 2. (c−f) Internal resistance R_{GC} obtained from IR drop in galvanostatic cycling as a function of current density j_{GC} and R_A, R_B, and R_C retrieved from EIS simulations for (c) case 1, (d) case 2, (e) case 5, and (f) case 8.

considered. Here, $\tau_D = L^2/D$ is the time scale for ion diffusion in the electrolyte and $\tau_{RC} = (R_\infty + R_D)C_{diff,eq}$ is the RC time constant for the electrolyte domain. Here, only the electrolyte domain was considered due to the fact that σ_e or R_e did not affect the slope k_{BC} (Figure 3). Figure 5b indicates that the slope k_{BC} was only a function of the ratio τ_D/τ_{RC}, regardless of the different parameters considered. In addition, the slope k_{BC} increased with increasing characteristic time ratio τ_D/τ_{RC}. This can be attributed to the fact that the behavior of the electrolyte deviated from an ideal equivalent RC circuit consisting of a resistor $R_\infty + R_D$ in series with a capacitor $C_{diff,eq}$ represented by a vertical line starting from point C (Figure 1). Deviation from such ideal equivalent RC circuit was due to ion diffusion in the electrolyte featuring time scale of $\tau_D = L^2/D$. In other words, the slope of the non-vertical line BC (Figure 1) can be used to indicate whether the charging process was controlled by EDL formation (large slope) or limited by ion diffusion in the electrolyte (small slope)

Differential Capacitance $C_{diff,eq}$. To retrieve the equilibrium differential capacitance from EIS simulations, one needs to first determine the low-frequency regime corresponding to the verti-

DOI: 10.1021/acs.jpcc.7b10582
J. Phys. Chem. C 2018, 122, 194−206

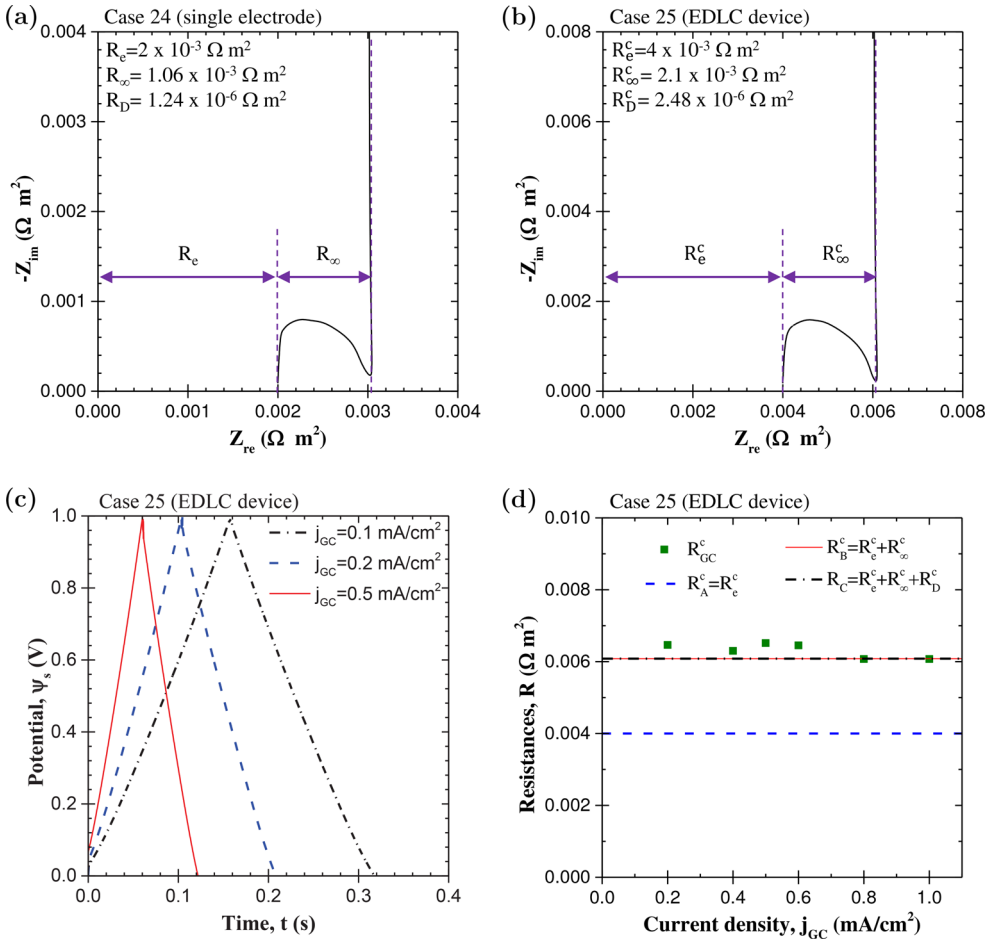

Figure 8. (a and b) Nyquist plots for (a) an EDLC electrode corresponding to case 24 (Table 2) and (b) an EDLC device (case 25) consisting of two identical electrodes described in case 24. (c) Potential $\psi_s(t)$ as a function of time for imposed current density j_{GC} of 0.1, 0.2, and 0.5 mA/cm^2 and (d) corresponding internal resistance R^c_{GC} obtained from IR drop in galvanostatic cycling as a function of current density j_{GC} and R^c_A, R^c_B, and R^c_C retrieved from EIS simulations for case 25.

cal line in the Nyquist plot. Figure 6a,b show the Nyquist plots of (a) case 16 and (b) case 18 (Table 2) for illustration purposes. Here, the vertical line indicates that the electrode can be approximated by a simplified RC circuit with a resistor in series with a capacitor.[16] Thus, the imaginary part Z_{im} of the complex impedance Z can be expressed as $Z_{im} = -1/(2\pi C_{diff,eq,EIS} f)$ where $C_{diff,eq,EIS}$ is the equilibrium differential capacitance retrieved from EIS simulations. Figure 6c,d shows $-Z_{im}$ as a function of $1/f$ for (c) Case 16 and (d) Case 18, respectively. They confirm that $-Z_{im}$ was proportional to $1/f$ with the coefficient of proportionality corresponding to $1/2\pi\ C_{diff,eq,EIS}$. Similar results were obtained for all 24 cases considered. In fact, Table 2 compares the equilibrium differential capacitance $C_{diff,eq,EIS}$ retrieved from low frequency EIS simulations, as illustrated in Figure 6c,d, and $C_{diff,eq}$ predicted by eq 13 for all 24 cases considered. The relative difference between the two approaches $e = |C_{diff,eq,EIS} - C_{diff,eq}|/C_{diff,eq}$ was less than 5% for all cases considered, confirming the validity of the retrieval method.

Comparison between Resistances from EIS and from Galvanostatic Cycling. Furthermore, Figure 7a,b shows the Nyquist plots and the potential $\psi_s(t)$ as a function of time under galvanostatic cycling for j_{GC} = 0.01 mA/cm^2 for cases 1, 2, 5, and 8 (Table 2). These four cases were chosen to study the effect of R_e and R_∞ on the internal resistance such that (i) cases 1, 2, and 5 featured the same bulk electrolyte resistance R_∞; (ii) cases 2 and 8 had the same electrode resistance R_e; and (iii) the sum $R_e + R_\infty$ was the same for cases 1 and 8. Moreover, Figure 7c−f shows the internal resistance R_{GC} retrieved from the "IR drop" estimated visually in galvanostatic cycling [eq 11] as well as $R_A = R_e$, $R_B = R_e + R_\infty$, and $R_C = R_e + R_\infty + R_D$ retrieved from the Nyquist plot (Figure 1) as functions of imposed current density j_{GC} in the range of 10^{-3}−0.01 mA/cm^2 for (c) case 1 and (d) case 2, (e) case 5, and (f) case 8. Figure 7 indicates that the internal resistance R_{GC} was nearly independent of the imposed current density j_{GC}. Moreover, R_{GC} agreed well with the sum of the electrode and electrolyte resistances, i.e., $R_{GC} = R_e + R_\infty$, for all four cases. The same conclusion was drawn from all 24 cases considered.

EDLC Devices. *Simulations.* Figure 8a,b compares the Nyquist plots for (a) an EDLC electrode (case 24) and (b) an EDLC device (case 25) consisting of two electrodes identical to that of case 24 separated by twice the electrolyte domain thickness. All electrode and electrolyte properties were identical for both cases, as summarized in Table 2. The Nyquist plots for a single electrode or for the EDLC device showed the same behavior. The real and the imaginary parts of the complex impedance of the device [Figure 8b] were equal to twice the values for the individual electrode [Figure 8a], for all frequencies considered. In addition, the resistance R^c_A of the device corresponded to twice the resistance of an individual electrode, i.e., $R^c_A = R^c_e = 2R_e$. Similarly, the resistance R^c_{AB} for the device was

DOI: 10.1021/acs.jpcc.7b10582
J. Phys. Chem. C 2018, 122, 194−206

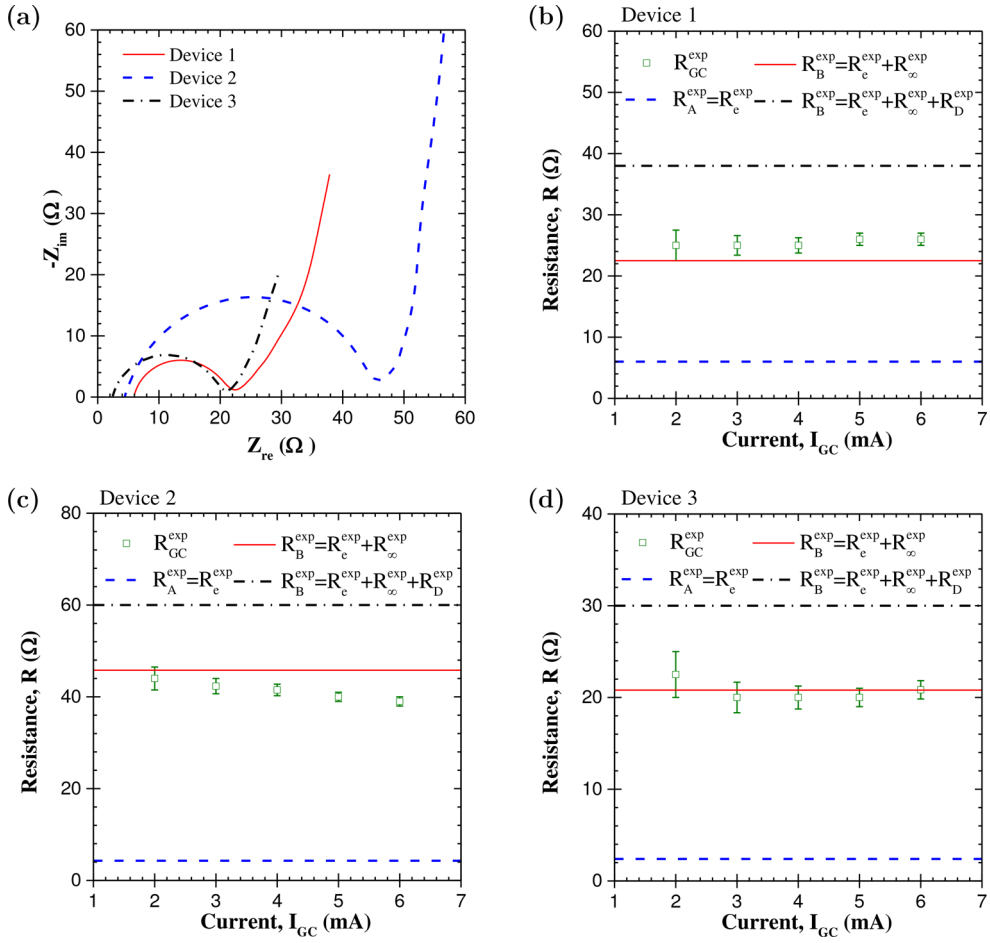

Figure 9. (a) Nyquist plots for the three experimental EDLC devices with activated carbon electrodes and different electrolytes (Table 3).[59] (b−d) Internal resistance R_{GC}^{exp} obtained experimentally from galvanostatic cycling as a function of current I_{GC} and R_A^{exp}, R_B^{exp}, and R_C^{exp} obtained from EIS measurement for (b) device 1, (c) device 2, and (d) device 3.

such that $R_{AB}^c = R_\infty^c = 2R_\infty$. In addition, the overlap of points B and C in both cases 24 and 25 was due to the small diffuse layer resistance R_D compared with R_∞. Indeed, the diffuse layer was thin compared with the relatively thick electrolyte domain due to the large ion concentration (c_∞ = 1 mol/L).

Moreover, Figure 8 also shows (c) the potential $\psi_s(t)$ as a function of time under galvanostatic cycling for j_{GC} = 0.01 mA/cm^2 and (d) the internal resistance R_{GC} retrieved from the "IR drop" in galvanostatic cycling [Figure 8c] as well as R_A, R_B, and R_C retrieved from the Nyquist plot [Figure 8b] as functions of imposed current density j_{GC} (0.1−1 mA/cm^2) for case 25. Figure 8d indicates that, here also, R_{GC} was in good agreement with resistance $R_B^c = R_e^c + R_\infty^c$ for simulations of two-electrode devices. Moreover, Table 2 compares the equilibrium differential capacitances $C_{diff,eq,EIS}$ retrieved from EIS and $C_{diff,eq}$ predicted by eq 13. The relative difference $e = |C_{diff,eq,EIS} - C_{diff,eq}|/C_{diff,eq}$ was less than 5% for both cases considered. Overall, this section confirmed that all interpretations of the Nyquist plots for single electrodes also apply to EDLC devices. In addition, the interpretations discussed previously should also be valid for EDLC devices with asymmetric electrolyte and/or nonidentical electrodes. Then, the resistances R_A, R_{AB}, and R_{BC} (Figure 1) would correspond to (i) the sum of the resistances of the positive and negative electrodes, (ii) the bulk electrolyte resistance, and (iii) the sum of the resistance of the two different diffuse layers near the positive and negative electrodes, respectively.

Experiments. Finally, Figure 9a shows experimental Nyquist plots for three different EDLC devices with footprint surface area of 1 cm^2 consisting of two identical electrodes made of 80 wt % activated carbon, 5 wt % TX100 as surfactant, 1.5 wt % carboxymethyl cellulose as thickening agent and binder, and 13.5 wt % styrene-butadiene rubber as binder with different electrolytes namely (i) 1 M $LiPF_6$/EC:DMC (1:1), (ii) 1 M citric acid/DI water, and (iii) 1 M TEATFB/acetonitrile. Note that different types of binders and surfactants can affect the resistance of the electrodes by changing particle-to-particle contact of activated carbon and affect the capacitance of the electrodes by changing the available carbon surface area. Details of the synthesis and characterization of the electrodes and of the EDLC devices were reported in ref 59 and need not be repeated. In brief, Table 3 summarized (i) the materials used for the electrode and electrolyte, (ii) the electrode R_e^{exp} and (iii) bulk electrolyte R_∞^{exp} resistances retrieved from the Nyquist plot based on the interpretations discussed previously, (iv) the internal resistance R_{GC} obtained from galvanostatic cycling as well as (v) the resistances R_A^{exp}, R_B^{exp}, and R_C^{exp}, and (vi) the equilibrium differential capacitance $C_{diff,eq,EIS}$ of the cell obtained from EIS measurements. The IR drop was visually estimated from the potential-time curve in galvanostatic cycling. In addition, the resistance R_C^{exp} was larger than the resistance measured at the lowest frequency due to the lack of a clear "vertical line" for low frequencies. Table 3 indicates that the sum of the electrode resistances R_e^{exp} was small and did

DOI: 10.1021/acs.jpcc.7b10582
J. Phys. Chem. C 2018, 122, 194−206

Table 3. Electrode Materials and Electrolyte Species, Operating Conditions, Resistance, and Capacitance Values of Devices in Experiments[59]

			potential window		current	resistances						capacitance
			ψ_{min}	ψ_{max}	I_{GC}	R_e^{exp}	R_∞^{exp}	R_{GC}^{exp}	R_A^{exp}	R_B^{exp}	R_C^{exp}	$C_{diff,eq,EIS}$
device	electrode	electrolyte	(V)	(V)	(mA)	(Ω)	(Ω)	(Ω)	(Ω)	(Ω)	(Ω)	(mF)
1	activated carbon	1 M $LiPF_6$ in EC:DMC (1:1)	0	1	2−6	6.0	16.5	22.5−27.5	6.0	22.5	>38.0	102.2
2	activated carbon	1 M citric acid in DI water	0	0.8	2−6	4.3	41.5	38.0−46.5	4.3	45.8	>60.0	117.7
3	activated carbon	1 M TEATFB in acetonitrile	0	1	2−6	2.4	18.4	18.3−25.0	2.4	20.8	>30.0	91.4

not vary significantly among the three devices. This is consistent with the fact that the electrodes of all three devices were nearly identical and made of activated carbon with a CMC binder.[59] In addition, the electrode resistance R_e^{exp} was small compared with that of the bulk electrolyte resistance R_∞^{exp}, which contributed the most to the internal resistance. Moreover, the bulk electrolyte resistance R_∞^{exp} for device 2 was much larger than that for devices 1 and 3. This can be attributed to the fact that citric acid is a weak electrolyte featuring low ionic conductivity.[59] Furthermore, Figure 9b−d shows the internal resistance R_{GC} retrieved from "IR drop" in galvanostatic cycling [eq 11] as a function of the imposed current I_{GC} (2−6 mA) as well as R_A^{exp}, R_B^{exp}, and R_C^{exp} retrieved from Nyquist plots for (b) device 1, (c) device 2, and (d) device 3. Figure 9 indicates that here also, R_{GC} was nearly independent of the imposed current I_{GC} and in good agreement with $R_B^{exp} = R_e^{exp} + R_\infty^{exp}$. These results were consistent with numerical simulations discussed previously.

Note that the present study considered only planar electrodes while practical EDLCs consist of porous electrodes. First, our simulations for planar electrodes could qualitatively reproduce experimental Nyquist plots for EDLCs with porous electrodes. This indicates that the model accounts for the key physical phenomena in EDLCs. However, accounting for porous electrodes is beneficial (i) to quantitatively reproduce experimental results and (ii) to investigate the effects of electrode architecture. The physical model discussed in the present study can be extended to porous electrodes in three-dimensional simulations but at significant computational cost.[66] Alternatively, the present study could be used to develop volume-averaged continuum models for porous electrodes accounting for the effects of EDL formation. Such models could identify the optimum operating conditions that maximize the capacitance and minimize the resistance of existing EDLC devices with porous electrodes. Note that for all cases, the continuum model is valid for pore or particle size larger than 5 nm, where the electrical and transport properties can be defined based on continuum theory. For pores less than 5 nm in diameter, the continuum model needs to be couple with (i) quantum mechanical models, such as density functional theory (DFT), and/or (ii) atomistic models, such as MD simulations for quantitative predictions. However, this falls outside the scope of the present study.

CONCLUSION

This study presented unequivocal physical interpretations of Nyquist plots from electrochemical impedance spectroscopy (EIS) for EDLC electrodes and devices without using an equivalent RC circuit. The Nyquist plots presenting the imaginary and real parts of the complex impedance of individual EDLC electrodes and devices were numerically reproduced based on the modified Poisson−Nernst−Planck model and closely resembled experimental measurements. This study established that the electrode resistance, bulk electrolyte resistance, diffuse layer resistance, and equilibrium differential capacitance can be retrieved directly from Nyquist plots. In addition, the internal resistance retrieved from the sum of electrode and bulk electrolyte resistances in EIS simulations showed good agreement with the internal resistance retrieved from the so-called "IR drop" in galvanostatic cycling. Finally, the above results and interpretations were confirmed experimentally for EDLC devices with electrodes made of activated carbon and various electrolytes.

ASSOCIATED CONTENT

Supporting Information

The Supporting Information is available free of charge on the ACS Publications website at DOI: 10.1021/acs.jpcc.7b10582.

Nomenclature of the variables used, governing equations, and initial and boundary conditions of the model. (ZIP)

AUTHOR INFORMATION

Corresponding Author

*E-mail: pilon@seas.ucla.edu. Phone: +1 (310) 206-5598. Fax: +1 (310) 206-2302.

ORCID

Bruce Dunn: 0000-0001-5669-4740

Laurent Pilon: 0000-0001-9459-8207

Notes

The authors declare no competing financial interest.

ACKNOWLEDGMENTS

The computation for this study was performed on the Hoffman2 cluster hosted by the Academic Technology Services (ATS) at the University of California, Los Angeles, U.S.A. This material is also based upon work supported, in part, by the China Scholarship Council (CSC). J.L. and B.D. greatly appreciate the support of this work by the Office of Naval Research.

REFERENCES

(1) Conway, B. E. *Electrochemical Supercapacitors: Scientific Fundamentals and Technological Applications*; Kluwer Academic/Plenum Publishers: New York, 1999.

(2) Kötz, R.; Carlen, M. Principles and Applications of Electrochemical Capacitors. *Electrochim. Acta* **2000**, *45*, 2483−2498.

(3) Taberna, P. L.; Simon, P.; Fauvarque, J. F. Electrochemical Characteristics and Impedance Spectroscopy Studies of Carbon-Carbon Supercapacitors. *J. Electrochem. Soc.* **2003**, *150*, 292−300.

(4) Segalini, J.; Daffos, B.; Taberna, P. L.; Gogotsi, Y.; Simon, P. Qualitative Electrochemical Impedance Spectroscopy Study of Ion Transport into Sub-nanometer Carbon Pores in Electrochemical Double Layer Capacitor Electrodes. *Electrochim. Acta* **2010**, *55*, 7489−7494.

(5) Miller, J. R.; Outlaw, R. A.; Holloway, B. C. Graphene Double-Layer Capacitor with AC Line-Filtering Performance. *Science* **2010**, *329*, 1637−1639.

DOI: 10.1021/acs.jpcc.7b10582
J. Phys. Chem. C 2018, 122, 194−206

(6) Zhu, Y.; et al. Carbon-Based Supercapacitors Produced by Activation of Graphene. *Science* **2011**, *332*, 1537−1541.
(7) Pech, M.; Brunet, D.; Durou, P.; Huang, H.; Mochalin, V.; Gogotsi, Y.; Taberna, P.; Simon, P. Ultrahigh-Power Micrometre-Sized Supercapacitors Based on Onion-like Carbon. *Nat. Nanotechnol.* **2010**, *5*, 651−654.
(8) Itoi, H.; Nishihara, H.; Kogure, T.; Kyotani, T. Three-Dimensionally Arrayed and Mutually Connected 1.2-nm Nanopores for High-performance Electric Double Layer. *J. Am. Chem. Soc.* **2011**, *133*, 1165−1167.
(9) Nilson, R. H.; Brumbach, M. T.; Bunker, B. C. Modeling the Electrochemical Impedance Spectra of Electroactive Pseudocapacitor Materials. *J. Electrochem. Soc.* **2011**, *158*, 678−688.
(10) Zhi, M.; Yang, F.; Meng, F.; Li, M.; Manivannan, A.; Wu, N. Effects of Pore Structure on Performance of an Activated-carbon Supercapacitor Electrode Recycled from Scrap Waste Tires. *ACS Sustainable Chem. Eng.* **2014**, *2*, 1592−1598.
(11) Levi, M. D.; Aurbach, D. Simultaneous Measurements and Modeling of the Electrochemical Impedance and the Cyclic Voltammetric Characteristics of Graphite Electrodes Doped with Lithium. *J. Phys. Chem. B* **1997**, *101*, 4630−4640.
(12) Mantia, F. L.; Vetter, J.; Novak, P. Impedance Spectroscopy on Porous Materials: A General Model and Application to Graphite Electrodes of Lithium-Ion Batteries. *Electrochim. Acta* **2008**, *53*, 4109−4121.
(13) Atebamba, J. M.; Moskon, J.; Pejovnik, S.; Gaberscek, M. On the interpretation of Measured Impedance Spectra of insertion Cathodes for Lithium-Ion Batteries. *J. Electrochem. Soc.* **2010**, *157*, 1218−1228.
(14) Murbach, M. D.; Schwartz, D. T. Extending Newman's Pseudo-Two-Dimensional Lithium-Ion Battery Impedance Simulation Approach to include the Nonlinear Harmonic Response. *J. Electrochem. Soc.* **2017**, *164*, E3311−E3320.
(15) He, Z.; Mansfeld, F. Exploring the Use of Electrochemical Impedance Spectroscopy (EIS) in Microbial Fuel Cell Studies. *Energy Environ. Sci.* **2009**, *2*, 215−219.
(16) Yuan, X. Z.; Song, C.; Wang, H.; Zhang, J. *Electrochemical Impedance Spectroscopy in PEM Fuel Cells: Fundamentals and Applications*; Springer-Verlag: London, 2010.
(17) Wang, Q.; Yan, J.; Wang, Y.; Wei, t.; Zhang, M.; Jing, X.; Fan, Z. Three-Dimensional Flower-like and Hierarchical Porous Carbon Materials as High-Rate Performance Electrodes for Supercapacitors. *Carbon* **2014**, *67*, 119−127.
(18) Farma, R.; Deraman, M.; Awitdrus, A.; Talib, I.; Taer, E.; Basri, N.; Manjunatha, J.; Ishak, M.; Dollah, B.; Hashmi, S. Preparation of Highly Porous Binderless Activated Carbon Electrodes from Fibres of Oil Palm Empty Fruit Bunches for Application in Supercapacitors. *Bioresour. Technol.* **2013**, *132*, 254−261.
(19) inal, I. I. G.; Holmes, S. M.; Banford, A.; Aktas, Z. the Performance of Supercapacitor Electrodes Developed from Chemically Activated Carbon Produced from Waste Tea. *Appl. Surf. Sci.* **2015**, *357*, 696−703.
(20) Li, W.; He, Q.; Pei, C.; Hou, B. Experimental and Theoretical Investigation of the Adsorption Behaviour of New Triazole Derivatives As Inhibitors for Mild Steel Corrosion in Acid Media. *Electrochim. Acta* **2007**, *52*, 6386−6394.
(21) Maocheng, Y.; Jin, X.; Libao, Y.; Tangqing, W.; Cheng, S.; Wei, K. EIS Analysis on Stress Corrosion Initiation of Pipeline Steel Under Disbonded Coating in Near-neutral pH Simulated Soil Electrolyte. *Corros. Sci.* **2016**, *110*, 23−34.
(22) Wang, H.; Shi, L.; Yan, T.; Zhang, J.; Zhong, Q.; Zhang, D. Design of Graphene-Coated Hollow Mesoporous Carbon Spheres as High Performance Electrodes for Capacitive Deionization. *J. Mater. Chem. A* **2014**, *2*, 4739−4750.
(23) Wang, H.; Zhang, D.; Yan, T.; Wen, X.; Zhang, J.; Shi, L.; Zhong, Q. Three-Dimensional Macroporous Graphene Architectures as High Performance Electrodes for Capacitive Deionization. *J. Mater. Chem. A* **2013**, *1*, 11778−11789.
(24) Bard, A. J.; Faulkner, L. R.; Leddy, J.; Zoski, C. G. *Electrochemical Methods: Fundamentals and Applications*; John Wiley & Sons: Hoboken, NJ, 1980; Vol. 2.
(25) Lasia, A. In *Modern Aspects of Electrochemistry, No. 32*; Conway, B. E., Bockris, J. O. M., White, R. E., Eds.; Kluwer Academic Publishers: New York, 2002; Chapter 2, pp 143−248.
(26) Orazem, M. E.; Tribollet, B. *Electrochemical Impedance Spectroscopy*; John Wiley & Sons: Hoboken, NJ, 2008.
(27) Yang, i.; Kim, S.-G.; Kwon, S. H.; Kim, M.-S.; Jung, J. C. Relationships Between Pore Size and Charge Transfer Resistance of Carbon Aerogels for Organic Electric Double-layer Capacitor Electrodes. *Electrochim. Acta* **2017**, *223*, 21−30.
(28) Coromina, H. M.; Adeniran, B.; Mokaya, R.; Walsh, D. A. Bridging the Performance Gap between Electric Double-Layer Capacitors and Batteries with High-Energy/High-Power Carbon Nanotube-Based Electrodes. *J. Mater. Chem. A* **2016**, *4*, 14586−14594.
(29) Yoo, H. D.; Jang, J. H.; Ryu, J. H.; Park, Y.; Oh, S. M. Impedance Analysis of Porous Carbon Electrodes to Predict Rate Capability of Electric Double-Layer Capacitors. *J. Power Sources* **2014**, *267*, 411−420.
(30) Lei, C.; Markoulidis, F.; Ashitaka, Z.; Lekakou, C. Reduction of Porous Carbon/Al Contact Resistance for an Electric Double-Layer Capacitor (EDLC). *Electrochim. Acta* **2013**, *92*, 183−187.
(31) Fang, B.; Binder, L. A Modified Activated Carbon Aerogel for High-Energy Storage in Electric Double Layers. *J. Power Sources* **2006**, *163*, 616−622.
(32) An, K. H.; Kim, W. S.; Park, Y. S.; Moon, J.-M.; Bae, D. J.; Lim, S. C.; Lee, Y. S.; Lee, Y. H. Electrochemical Properties of High-Power Supercapacitors Using Single-Walled Carbon Nanotube Electrodes. *Adv. Funct. Mater.* **2001**, *11*, 387−392.
(33) Arulepp, M.; Permann, L.; LEIS, J.; Perkson, A.; Rumma, K.; Jänes, A.; Lust, E. influence of the Solvent Properties on the Characteristics of a Double Layer Capacitor. *J. Power Sources* **2004**, *133*, 320−328.
(34) Liu, C.-L.; Dong, W.-S.; Cao, G.-P.; Song, J.-R.; Liu, L.; Yang, Y.-S. Influence of KOH Followed By Oxidation Pretreatment on the Electrochemical Performance of Phenolic Based Activated Carbon Fibers. *J. Electroanal. Chem.* **2007**, *611*, 225−231.
(35) Gamby, J.; Taberna, P.; Simon, P.; Fauvarque, J.; Chesneau, M. Studies and Characterisations of Various Activated Carbons used for Carbon/Carbon Supercapacitors. *J. Power Sources* **2001**, *101*, 109−116.
(36) Portet, C.; Yushin, G.; Gogotsi, Y. Electrochemical Performance of Carbon Onions, Nanodiamonds, Carbon Black and Multiwalled Nanotubes in Electrical Double Layer Capacitors. *Carbon* **2007**, *45*, 2511−2518.
(37) Lufrano, F.; Staiti, P.; Minutoli, M. Evaluation of Nafion Based Double Layer Capacitors By Electrochemical Impedance Spectroscopy. *J. Power Sources* **2003**, *124*, 314−320.
(38) Nian, Y.-R.; Teng, H. Influence of Surface Oxides on the Impedance Behavior of Carbon-based Electrochemical Capacitors. *J. Electroanal. Chem.* **2003**, *540*, 119−127.
(39) Kang, J.; Jayaram, S. H.; Rawlins, J.; Wen, J. Characterization of Thermal Behaviors of Electrochemical Double Layer Capacitors (EDLCs) with Aqueous and Organic Electrolytes. *Electrochim. Acta* **2014**, *144*, 200−210.
(40) Kang, J.; Atashin, S.; Jayaram, S. H.; Wen, J. Z. Frequency and Temperature Dependent Electrochemical Characteristics of Carbon-based Electrodes Made of Commercialized Activated Carbon, Graphene and Single-Walled Carbon Nanotube. *Carbon* **2017**, *111*, 338−349.
(41) Conway, B. E.; Pell, W. G. Power Limitations of Supercapacitor Operation Associated with Resistance and Capacitance Distribution in Porous Electrode Devices. *J. Power Sources* **2002**, *105*, 169−181.
(42) Yoon, S.; Jang, J. H.; Ka, B. H.; Oh, S. M. Complex Capacitance Analysis on Rate Capability of Electric-Double Layer Capacitor (EDLC) Electrodes of Different Thickness. *Electrochim. Acta* **2005**, *50*, 2255−2262.
(43) Bohlen, O.; Kowal, J.; Sauer, D. Ageing Behaviour of Electrochemical Double Layer Capacitors: Part I. Experimental Study and Ageing Model. *J. Power Sources* **2007**, *172*, 468−475.
(44) Yoon, S.; Lee, C. W.; Oh, S. M. Characterization of Equivalent Series Resistance of Electric Double-Layer Capacitor Electrodes Using Transient Analysis. *J. Power Sources* **2010**, *195*, 4391−4399.

DOI: 10.1021/acs.jpcc.7b10582
J. Phys. Chem. C 2018, 122, 194−206

(45) Kaus, M.; Kowal, J.; Sauer, D. U. Modelling the Effects of Charge Redistribution During Self-Discharge of Supercapacitors. *Electrochim. Acta* **2010**, *55*, 7516−7523.
(46) Spyker, R.; Nelms, R. Classical Equivalent Circuit Parameters for a Double-layer Capacitor. *IEEE Trans. Aerosp. Electron. Syst.* **2000**, *36*, 829−836.
(47) Bazant, M. Z.; Thornton, K.; Ajdari, A. Diffuse-Charge Dynamics in Electrochemical Systems. *Phys. Rev. E* **2004**, *70*, 021506.
(48) Olesen, L. H.; Bazant, M. Z.; Bruus, H. Strongly Nonlinear Dynamics of Electrolytes in Large AC Voltages. *Phys. Rev. E* **2010**, *82*, 011501.
(49) Chu, K. T.; Bazant, M. Z. Nonlinear Electrochemical Relaxation around Conductors. *Phys. Rev. E* **2006**, *74*, 011501.
(50) Cahan, B. D.; Chen, C.-T. the Nature of the Passive Film on Iron II. A-C Impedance Studies. *J. Electrochem. Soc.* **1982**, *129*, 474−480.
(51) Shi, L.; Crow, M. Comparison of ultracapacitor electric circuit models. Power and Energy Society General Meeting-Conversion and Delivery of Electrical Energy in the 21st Century, 2008 IEEE. 2008; pp 1−6.
(52) Barthel, J. M.; Krienke, H.; Kunz, W. *Physical Chemistry of Electrolyte Solutions: Modern Aspects*; Springer Science & Business Media: Berlin, 1998; Vol. *5*.
(53) Wang, H.; Thiele, A.; Pilon, L. Simulations of Cyclic Voltammetry for Electric Double Layers in Asymmetric Electrolytes: A Generalized Modified Poisson-Nernst-Planck Model. *J. Phys. Chem. C* **2013**, *117*, 18286−18297.
(54) Masliyah, J. H.; Bhattacharjee, S. *Electrokinetic and Colloid Transport Phenomena*; John Wiley & Sons: Hoboken, NJ, 2006.
(55) Wang, H.; Pilon, L. Intrinsic Limitations of Impedance Measurements in Determining Electric Double Layer Capacitances. *Electrochim. Acta* **2012**, *63*, 55−63.
(56) Wang, H.; Pilon, L. Mesoscale Modeling of Electric Double Layers with Three-Dimensional Ordered Structures. *J. Power Sources* **2013**, *221*, 252−260.
(57) Janz, G. J.; Tomkins, R. P. T. *Nonaqueous Electrolytes Handbook*; Academic Press: New York, 1972; Vol. *I*.
(58) Woo, S. W.; Dokko, K.; Nakano, H.; Kanamura, K. Preparation of Three Dimensionally Ordered Macroporous Carbon with Mesoporous Walls for Electric Double-Layer Capacitors. *J. Mater. Chem.* **2008**, *18*, 1674−1680.
(59) Munteshari, O.; Lau, J.; Krishnan, A.; Dunn, B.; Pilon, L. Isothermal Calorimeter for Measurements of Time-Dependent Heat Generation Rate in Individual Supercapacitor Electrodes. *J. Power Sources* **2018**, *374*, 257−268.
(60) Burke, a.; Miller, M. Testing of Electrochemical Capacitors: Capacitance, Resistance, Energy Density, and Power Capability. *Electrochim. Acta* **2010**, *55*, 7538−7548.
(61) Zhao, S.; Wu, F.; Yang, L.; Gao, L.; Burke, a. F. A Measurement Method for Determination of DC Internal Resistance of Batteries and Supercapacitors. *Electrochem. Commun.* **2010**, *12*, 242−245.
(62) Bagotsky, V. S. *Fundamentals of Electrochemistry*, 2nd ed.; John Wiley & Sons: Hoboken, NJ, 2006.
(63) Kilic, M. S.; Bazant, M. Z.; Ajdari, A. Steric Effects in the Dynamics of Electrolytes At Large Applied Voltages. II. Modified Poisson-Nernst-Planck Equations. *Phys. Rev. E* **2007**, *75*, 021503.
(64) Kornyshev, A. A. Double-Layer in Ionic Liquids: Paradigm Change? *J. Phys. Chem. B* **2007**, *111* (20), 5545−5557, DOI: 10.1021/jp067857o.
(65) Wang, H.; Fang, J.; Pilon, L. Scaling Laws for Carbon-Based Electric Double Layers. *Electrochim. Acta* **2013**, *109*, 316−321.
(66) Mei, B.-A.; Pilon, L. Three-Dimensional Cyclic Voltammetry Simulations of EDLC Electrodes Made of Ordered Carbon Spheres. *Electrochim. Acta* **2017**, *255*, 168−178.

DOI: 10.1021/acs.jpcc.7b10582
J. Phys. Chem. C 2018, 122, 194−206